www.MaterialsViews.com

ADVANCED
ENERGY
MATERIALS
www.advenergymat.de

COMMUNICATION

Efficient Semitransparent Perovskite Solar Cells for 23.0%-Efficiency Perovskite/Silicon Four-Terminal Tandem Cells

Bo Chen, Yang Bai, Zhengshan Yu, Tao Li, Xiaopeng Zheng, Qingfeng Dong, Liang Shen, Mathieu Boccard, Alexei Gruverman, Zachary Holman, and Jinsong Huang*

Emerging organic–inorganic hybrid perovskite solar cells (PSCs) distinguish themselves among photovoltaic devices as excellent top cell candidates for high-efficiency silicon-based tandem devices. Due to their excellent light absorption and large electron and hole diffusion lengths, PSCs have reached certified efficiencies as high as 22.1% within six years of research.[1–8] Moreover, perovskite light absorbers have bandgaps that may be tuned over a wide range from 1.17 to 3.1 eV which facilitates bandgap optimization for high efficiency perovskite/Si tandem cells.[9–18] Another advantage of PSCs is that polycrsytalline perovskite thin films can be made on various substrates by low-temperature solution processes.[19–24]

Perovskite/Si tandem cells offer an attractive path to increase the efficiency of perovskite and silicon cells beyond the single-junction Shockley–Queisser limit without adding significant cost to silicon solar cells.[25–34] The perovskite top cell in a perovskite/Si tandem requires a transparent front electrode that must have both high transparency and good conductivity; in addition, the rear electrode must be transparent to near-infrared light since this light will be converted to electricity with high efficiency in the silicon bottom cell if it is not parasitically absorbed first. Several researches have reported four-terminal and monolithically integrated two-terminal tandem configurations with different types of transparent electrodes for PSCs.[25–34] Bailie et al. utilized a transparent silver nanowire electrode on PSCs to achieve a 12.7%-efficient semitransparent perovskite cell.[25] However, the diffusion of silver into the perovskite and charge transport layers leads to device degradation.[31,35] Transparent conductive oxides (TCOs), such as indium tin oxide (ITO), hydrogen-doped indium oxide (IO:H),

aluminum-doped zinc oxide (ZnO:Al), and indium zinc oxide (IZO) deposited by sputtering have also been investigated as transparent electrode for perovskite/Si tandem cells,[27–33] with efficiencies of up to 14.5% for semitransparent perovskite cells and 21.2% for tandem cells.[30] The sputtering process damages the perovskite and charge transport layers,[27–33] consequently, buffer layers made of inorganic materials such as molybdenum oxide (MoO_x), ZnO:Al, and ITO nanoparticles are often inserted before sputtering to protect the perovskite and charge transport layers.[27–33] Ultrathin metal films (<10 nm thick) deposited by thermal evaporation could be alternative transparent electrodes that would not require buffer layers,[36–38] as evaporation causes much less damage than sputtering. However, such electrodes have not yet been thoroughly exploited in perovskite cells; the highest reported efficiency for a semitransparent PSC utilizing a metal film is 11.5%.[36]

In this study, we developed ultrathin metal electrodes with a combination of good optical transparency and electrical conductivity. By controlling the roughness of the perovskite and charge transport layers and growing continuous ultrathin metal films with a metal wetting layer, we show a record efficiency of 16.5% for a semitransparent PSC. When a semitransparent PSC is stacked atop a near-infrared-enhanced silicon heterojunction solar cell, the silicon cell is measured to have 6.5% efficiency, yielding a summed efficiency of 23.0%, which is higher than both the silicon and perovskite sub-cells.

There are three key requirements for a transparent metal electrode in an efficient semitransparent PSC: (1) it should not react with the underlying perovskite layer and charge transport layers, (2) it should have high transmittance for incident sunlight, and (3) it should have good conductivity for charge collection. A challenge is that there is always a trade-off between transparency and conductivity for any transparent electrode. Here, we fixed the thickness of the metal films at 8 nm and evaluated their transparency and conductivity when deposited on glass and perovskite cell. Several metals have been investigated as electrode materials in perovskite solar cells, such as Au, Ag, Al, and Cu.[21–23,39–44] In a previous study, we found that Cu and Au had much better stability than Ag and Al when in direct contact with the perovskite films under ambient atmosphere,[40] and thus Cu and Au were chosen as the metal electrode candidates in this study. An 8 nm thick Cu film maintained a decent conductivity of 28 Ω sq^{-1}; however, as shown in **Figure 1**c, its transmittance is poor in the near infrared range. An 8 nm thick Au layer, by contrast, displayed low conductivity due to the formation of a discontinuous film on

Dr. B. Chen, Dr. Y. Bai, X. Zheng, Dr. Q. Dong,
Dr. L. Shen, Prof. J. Huang
Department of Mechanical and Materials Engineering
University of Nebraska-Lincoln
Lincoln, NE 68588, USA
E-mail: jhuang2@unl.edu
Z. Yu, Dr. M. Boccard, Prof. Z. Holman
School of Electrical
Computer, and Energy Engineering
Arizona State University
Tempe, AZ 85287, USA
Dr. T. Li, Prof. A. Gruverman
Department of Physics and Astronomy
University of Nebraska-Lincoln
Lincoln, NE 68588, USA

**ADVANCED
ENERGY
MATERIALS**
www.advenergymat.de

*Materials
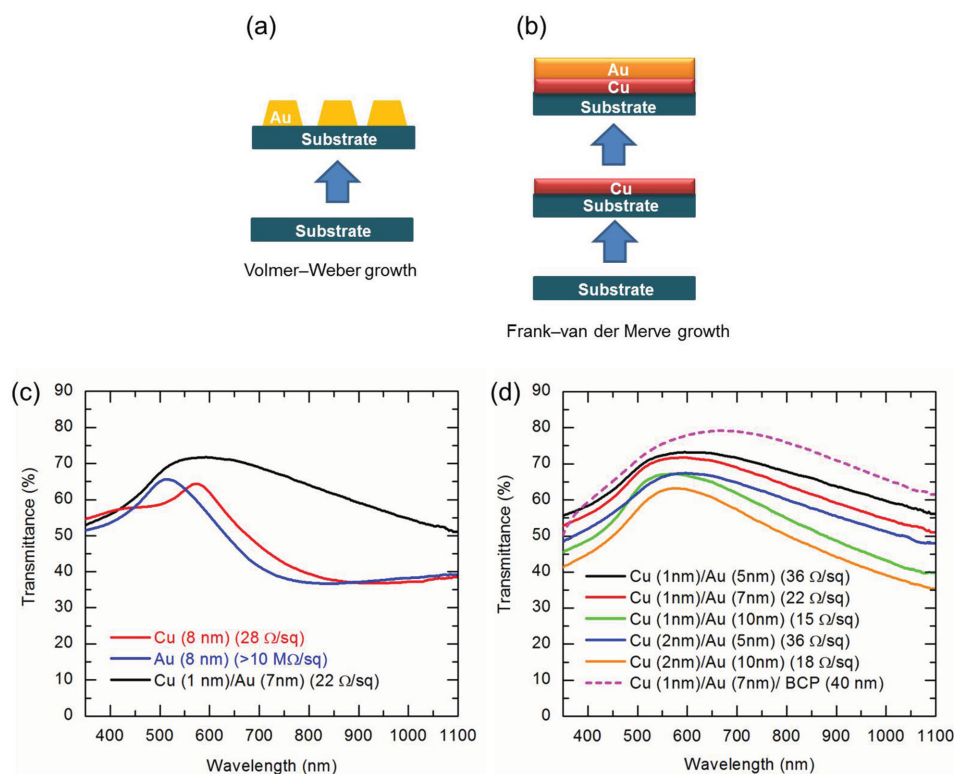Views*
www.MaterialsViews.com

Figure 1. Schematic illustration of a) island growth of Au on a glass substrate and b) layer-by-layer growth of Au on a Cu-coated glass substrate. c) Transmittance and conductivity of an 8 nm thick pristine Cu film, an 8 nm thick pristine Au film, and a 7 nm thick Au film with a 1 nm thick Cu seed layer on glass substrate. d) Transmittance and conductivity of different Cu-seeded Au films on glass substrate.

glass and perovskite cell (Figure S1, Supporting Information). Au atoms are more strongly coupled to each other than to the substrate, which leads to formation of Au islands via Volmer–Weber growth during thermal evaporation (Figure 1a). As Cu has a much higher surface energy of 1790 mJ m^{-2} than Au (1506 mJ m^{-2}),[45] we introduced a 1 nm thick Cu seed layer to improve the Au wettability. As a result, Au atoms attach preferentially to the Cu surface rather than to each other, which leads to Frank–van der Merve growth and the formation of continuous ultrathin Au films (Figure 1b). As shown in Figure 1c, a 7 nm thick Au film on a 1 nm thick Cu seed layer (Cu (1 nm)/Au (7 nm)) demonstrates higher transmittance and better conductivity than pristine 8 nm thick Au and Cu films. Compared with a Cu (1 nm)/Au (7 nm) electrode, a Cu (1 nm)/Au (5 nm) electrode improved the transparency but greatly increased the sheet resistance from 22 to 36 Ω sq^{-1}; on the other hand, a Cu (1 nm)/Au (10 nm) film had better conductivity but significantly sacrificed transparency (Figure 1d). Increasing the thickness of the Cu seed layer from 1 to 2 nm did not alter the electrode conductivity but predictably decrease its transparency. Therefore, the Cu (1 nm)/Au (7 nm) layer stack was chosen as the optimum semitransparent electrode for use in PSCs.

When incorporated into a perovskite solar cell, the metal electrode is deposited at last. Because it is only 8 nm thick, the surface roughness of the perovskite light absorber and charge transport layers may dramatically influence its continuity and thus its conductivity and transparency. The roughness of the perovskite layer, in turn, varies with the process used to form

the perovskite film. A MAPbI$_3$ film fabricated by the two-step interdiffusion approach displays a surface roughness of 21.7 nm.[24] Compared to 22 Ω sq^{-1} on a glass substrate, the sheet resistance of a Cu (1 nm)/Au (7 nm) electrode on two-step MAPbI$_3$ films increases to 40 Ω sq^{-1}, which is much larger than the 16 Ω sq^{-1} sheet resistance of ITO substrate for perovskite cell. In order to reduce the roughness of the perovskite layer, we utilized a one-step spin extraction approach that is similar to previously reported processes, but the mixed solvents were changed to dimethylformamide (DMF) and dimethyl sulfoxide (DMSO).[22,46,47] While spin-coating the MAPbI$_3$ precursor solution, toluene was dropped to quickly precipitate MAPbI$_3$ so that very smooth films formed, as shown by the scanning electron microscopy (SEM) cross-section in **Figure 2**e. After thermal annealing at 100 °C for 10 min, the one-step MAPbI$_3$ film had a surface roughness of 12.4 nm, as revealed by the atomic force microscopy (AFM) topography imaging shown in Figure 2a. This is almost half that of two-step MAPbI$_3$ films. Covering the perovskite films with a PCBM/C$_{60}$/BCP layer stack, which is needed for high device efficiency,[40,41] the surface roughness further reduced to 6.1 nm (Figure 2b). The semitransparent Cu (1 nm)/Au (7 nm) metal electrode on this smooth MAPbI$_3$ perovskite device is continuous (Figure 2c,d) and has a sheet resistance of 23 Ω sq^{-1}, which is close to the ITO top electrode. Finally, another 40 nm thick BCP layer was added on top of the Cu (1 nm)/Au (7 nm) film to further improve the transmittance of the semitransparent electrode; BCP has been shown to enhance the transparency by around 10% in the near-infrared range (Figure 1d).
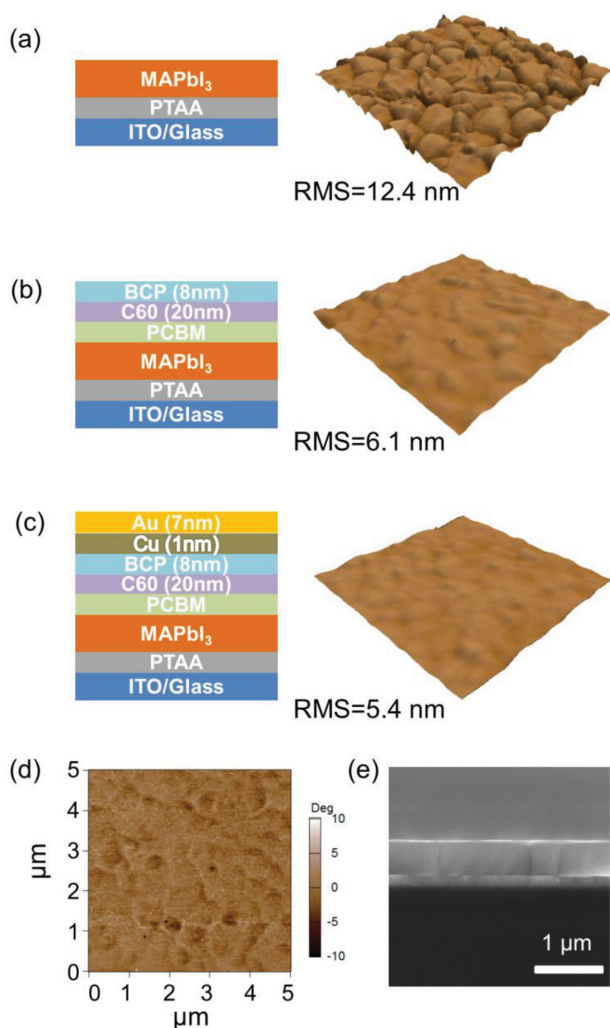
www.MaterialsViews.com

ADVANCED
ENERGY
MATERIALS
www.advenergymat.de

COMMUNICATION

Figure 2. Schematic drawing and AFM topography image of a a) MAPbI$_3$ film on PTAA-coated ITO/glass, b) PCBM/C$_{60}$/BCP coated MAPbI$_3$ film, and c) PCBM/C$_{60}$/BCP coated MAPbI$_3$ film after deposition of a Cu (1 nm)/Au (7 nm) electrode. The image sizes are 5 μm × 5 μm. The surface roughness is revealed by the root mean square (RMS) value. d) Corresponding AFM phase image of (c). e) SEM cross-section of a MAPbI$_3$ film on PTAA-coated ITO/glass.

We fabricated semitransparent perovskite solar cells using 500 nm thick smooth MAPbI$_3$ films. An opaque control device with an 80 nm thick Cu electrode displayed a respectable efficiency of 19.4% due to crystalline grains ≈1 μm in size formed with the help of DMSO additives and due to excellent passivation of the perovskite surfaces and grain boundaries by double fullerene layers.[22,48,49] Without the DMSO in the precursor solution yield the MAPbI$_3$ film with grain size 300–400 nm, and the surface is much rougher than the mixed solvent of DMF and DMSO (Figure S2, Supporting Information). When illuminated through the glass/ITO side (denoted as front illumination), the semitransparent cell had a short-circuit current density (J_{SC}) of 20.6 mA cm^{-2}, fill factor (FF) of 74.1%, open-circuit voltage (V_{OC}) of 1.08 V, and power conversion efficiency (PCE) of 16.5% (**Figure 3**a). The efficiency was confirmed by the

stable photocurrent and power output at the maximum power point (0.87 V bias) for 1000 s, as shown in Figure 3b. The semitransparent perovskite solar cells have excellent stability when store under the dry inert atmosphere as shown in Figure S3 of the Supporting Information. When illuminated from the Cu/Au/BCP side (denoted as rear illumination), the device had 12.1% efficiency with a reduced J_{SC} of 15.2 mA cm^{-2} because the Cu/Au/BCP layer is less transparent in the visible spectrum than the ITO front electrode. Note that the semitransparent perovskite solar cells had hysteresis-free behavior, as seen by the forward and reverse current–voltage (J–V) scans in Figure 3a, which is again ascribed to the fullerene passivation effect as we previously reported.[49] A series resistance of 6.4 Ω cm^2 was calculated from the semitransparent cell under front illumination J–V characteristic. This small series resistance and corresponding high FF further illustrate that the Cu/Au semitransparent electrodes induce little loss during collection and lateral transport of photogenerated charges.

Semitransparent PSCs under front illumination have lower PCE than opaque control devices mainly because of reduced J_{SC}. As shown in Figure 3c, semitransparent perovskite solar cells under front illumination and opaque cells have comparable external quantum efficiency (EQE) values at short wavelengths (300–550 nm), but semitransparent cells have smaller EQE at longer wavelengths (600–800 nm). From the extinction coefficient (κ),[50] more than 500 nm of MAPbI$_3$ film is required to absorb 95% of the photons in the 600–800 nm wavelength range (Figure 3d), but the MAPbI$_3$ layer used here is only 500 nm thick. In the opaque PSC, the thick (80 nm) Cu electrode serves as a rear reflector that increases the path length of light inside the perovskite layers, and this benefits the harvesting of long-wavelength photons. In the semitransparent PSC, the transmittance of these nonabsorbed photons leads to J_{SC} loss, but they will be absorbed in silicon bottom cell in tandem devices.

Amorphous silicon/crystalline silicon heterojunction cells are excellent candidates for silicon-based tandem devices because they have high V_{OC} resulting from the separation of the highly recombination-active (Ohmic) contacts from the silicon absorber bulk.[51] To improve the silicon bottom cell performance for tandem configurations, we fabricated infrared-enhanced silicon heterojunction cells (IR cells) by applying a double-layer antireflection coating at the front side and a MgF$_2$ back reflector layer at the rear side, as illustrated in **Figure 4**a. As in 1 sun silicon heterojunction cells,[51] intrinsic and doped a-Si:H layers were deposited on a textured n-type monocrystalline wafer. On the front side, conventional ITO was replaced by IZO as a lateral transport layer because IZO has a higher carrier mobility.[52] IZO typically has a lower carrier concentration than ITO and thus higher sheet resistance, but this is desirable in tandems because lower carrier density (and higher mobility) can decrease free-carrier absorption induced parasitic loss of near-infrared light. The high sheet resistance of IZO is not an issue in here. Because the absolute power loss caused by sheet resistance is proportional to the product of J_{mpp} and the sheet resistance,[53] while the J_{mpp} in the bottom cell of a perovskite/silicon four-terminal tandem is roughly one-third of the 1 sun J_{mpp} of the silicon cell because the light is filtered through the perovskite, and thus the front TCO layer can be three times
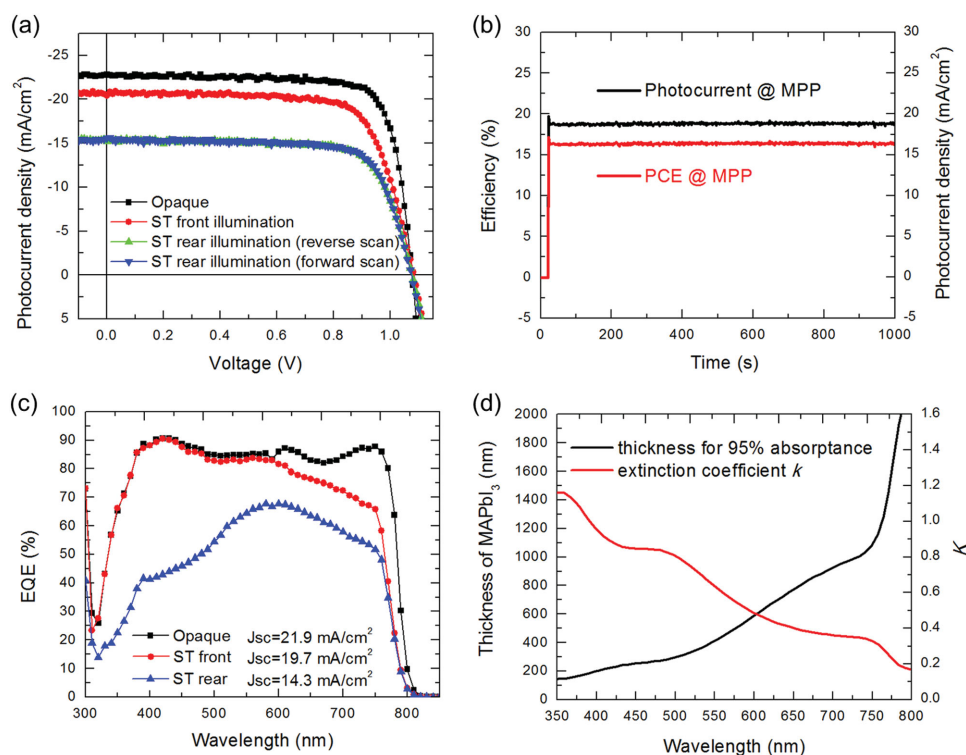
ADVANCED
ENERGY
MATERIALS

www.advenergymat.de

Makrials
Views

www.MaterialsViews.com

Figure 3. a) J–V curves of an opaque PSC and semitransparent (ST) PSC under front illumination and rear illumination with reverse and forward scans. b) Measured photocurrent density and PCE at the maximum power point (MPP) with 0.87 V bias for semitransparent PSCs under front illumination. c) EQE curves for opaque and semitransparent PSCs under front and rear illumination. d) Extinction coefficient κ and required depth for a MAPbI$_3$ film to absorb 95% of light at different wavelengths.

more resistive with the same power loss.[53] The 50 nm thick IZO layer was coated with 120 nm of SiO$_x$; together, they served as a dual-layer antireflection coating that better transmits near-infrared light. On the rear side of the cell, a 15 nm thick ITO layer was deposited over the entire surface, followed by a 300 nm thick MgF$_2$ layer that was evaporated through a stainless-steel mesh to define local openings. Finally, a silver layer was sputtered on the rear surface. Because of the MgF$_2$ patterning, the silver contacts the ITO in the (≈5%) area without MgF$_2$, whereas it remains separated from the ITO and wafer everywhere else. Inserting the MgF$_2$ layer between the silver and silicon increases rear internal reflectance by reducing the fraction of light that reaches the lossy silver reflector. It does this by both limiting the transmission cone at the silicon rear surface and suppressing plasmonic absorption of light arriving outside of the cone.[54–56]

The performance of a silicon IR cell can be evaluated by the total absorbance (1-reflection) and EQE curves in Figure 4b. Compared to the reference cell (which uses only ITO on the front, and no MgF$_2$ on the back), the IR cell had a J_{SC} only 0.5 mA cm^{-2} higher for wavelengths <700 nm. However, in the near-infrared region of the spectrum (700–1200 nm), where the perovskite top cell is transparent and the silicon cell performance matters, the J_{SC} improvement is

considerable: 22.7 mA cm^{-2} compared to 21.1 mA cm^{-2}. This gain results from the aforementioned design alterations that minimize parasitic absorption of near-infrared light. The total absorbance (1-reflection) spectra in Figure 4b confirm this: Only 45% of 1200 nm light, which silicon does not absorb, is absorbed in the IR cell (by, e.g., the TCO and silver). By contrast, 82% is absorbed in the reference cell. As a result of the very small near-infrared parasitic absorption in the IR cell, the gap between the EQE and total absorbance curves is
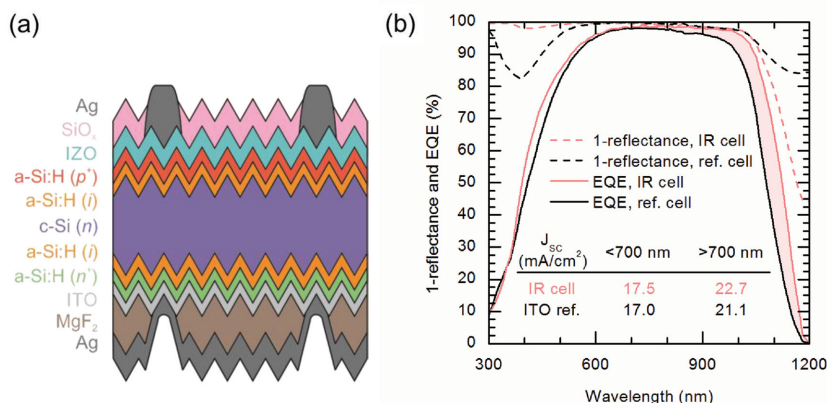

Figure 4. a) Schematic of the infrared-enhanced silicon heterojunction cell. b) Total absorbance (1-reflectance) and EQE spectra of infrared-enhanced and reference silicon heterojunction cells. The shaded area indicates the improvement in near-infrared performance resulting from the double-layer antireflection coating and MgF$_2$ layer.

www.MaterialsViews.com

ADVANCED
ENERGY
MATERIALS
www.advenergymat.de

COMMUNICATION

approaching zero, as is expected when all the light absorbed is absorbed within the silicon wafer and thus converted into photogenerated carriers. An IR cell with an area of 4 cm², measured alone at 1 sun, had a PCE of 21.2% with a V_{OC} of 716 mV and FF of 75.6%; the reference cell had a PCE of 20.1%.

Combining the high efficiency semitransparent PSCs and infrared-enhanced silicon heterojunction cells, we evaluated the potential for perovskite/Si tandem cells in the four-terminal configuration by measuring the silicon cell under light filtered with a perovskite cell. The characterization was carried out independently for each sub-cell. Following the results in Figure 3, front illumination of the semitransparent PSCs was used for best performance. As shown in **Figure 5**a, most visible light was absorbed by the perovskite top cell, with 10%–20% of red light (600–700 nm) transmitted to the bottom cell. The light absorption around 800 and 1020 nm above the bandgap of perovskite film is come from the absorption of semitransparent electrode, similar phenomena has also been reported in the sputtered ITO electrode.[30] For near-infrared light, 10%–20% light was also reflected by the semitransparent PSC, together with 15%–30% absorption, it left ≈60% of near-infrared light for the silicon IR cell. The J–V curves and EQE spectra of the semitransparent PSC and filtered silicon IR cell are shown in Figure 5b,c, and device performance is summarized in **Table 1**. After the light is filtered by the perovskite top cell, the J_{SC} and V_{OC} of the silicon bottom cell are expected to decrease because of the reduced light intensity, and the FF is expected to increase because of the reduced effect of series resistance at lower illumination. The filtered silicon IR cell exhibited a V_{OC} of 679 mV, a J_{SC} of 12.3 mA cm⁻², and a FF of 77.9% for a PCE of 6.5%. Adding the 16.5% efficiency from the perovskite top cell, this corresponds to a summed efficiency of 23.0%. This is substantially higher than those of both the optimized silicon IR cell and the opaque perovskite cell.

The reference PSC used in here only has power conversion efficiency of 19.4%, and the semitransparent top cell can obtain 16.5% PCE with the Cu (1 nm)/Au (7 nm) electrode, which remain 85% performance of the opaque reference cell. If apply this semitransparent metal electrode onto the highest reported 22.1% PSC, we can expect 18.8% power conversion efficiency for the top perovskite cell. Together with 6.5% infrared-enhanced silicon bottom cell, we should obtain ≈25% overall efficiency for the four terminal perovskite/Si device.

In summary, we have investigated semitransparent perovskite solar cells and infrared enhanced silicon heterojunction cells for high-efficiency tandem devices. A semitransparent metal electrode with good electrical conductivity and optical transparency has been fabricated by thermal evaporation of 7 nm of Au onto a 1 nm thick Cu seed layer. For this electrode to reach its full potential, MAPbI₃ thin films were formed by a modified one-step spin-coating method, resulting in a smooth layer that allowed the subsequent metal thin film to remain continuous. The fabricated semitransparent perovskite solar cells demonstrated 16.5% efficiency under 1 sun illumination, and were coupled with infrared-enhanced silicon heterojunction cells tuned specifically for perovskite/Si tandem devices. A double-layer antireflection coating at the front side and MgF₂ reflector at rear side of the silicon heterojunction cells reduced parasitic absorption of near-infrared
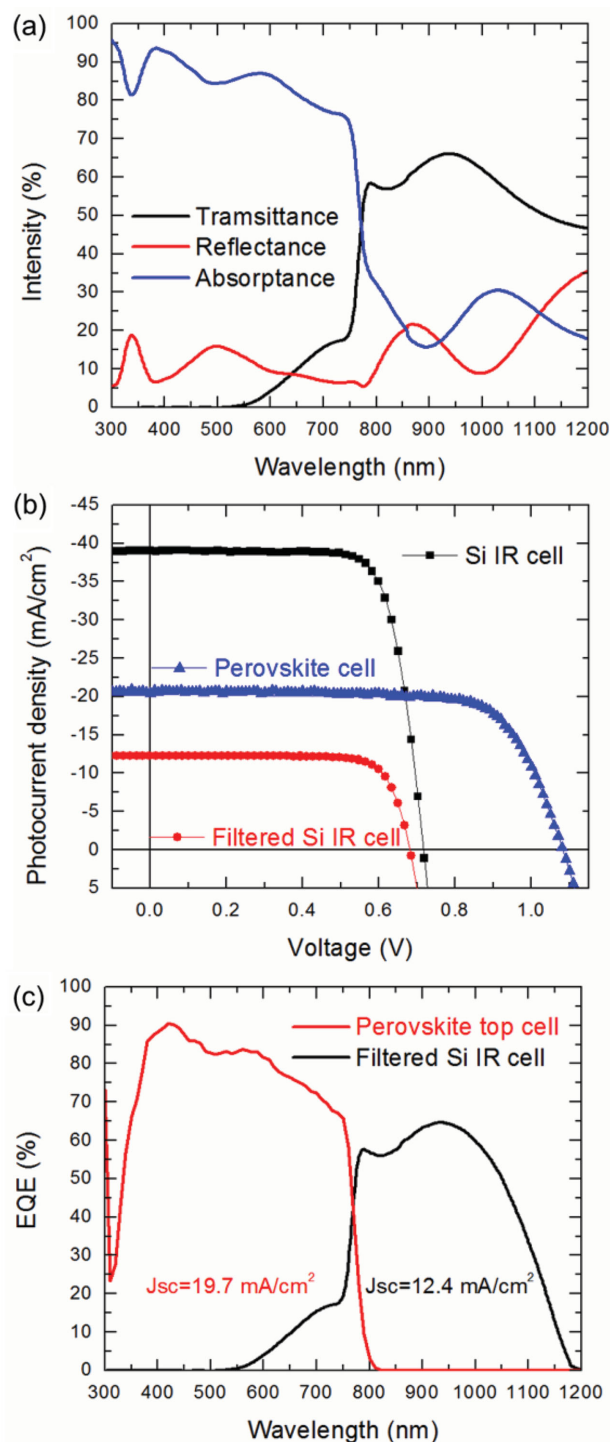

Figure 5. a) Transmittance, reflectance, and absorptance of a semitransparent PSC under front illumination. b) J–V curves of a semitransparent PSC under front illumination and a silicon IR cell with and without the semitransparent PSC filter. c) EQE spectra of semitransparent PSC top and filtered silicon IR bottom cells.

light, leading to 6.5% efficiency after filtering with a perovskite device and 23.0% summed efficiency for the perovskite/Si tandem device.

COMMUNICATION

Table 1. Summary of photovoltaic parameters for a semitransparent perovskite top cell, silicon IR cell, filtered silicon IR cell, and the overall four-terminal perovskite/Si tandem cell.

Device	V_{OC} [V]	J_{SC} [mA cm^{-2}]	FF [%]	PCE [%]
ST-PSC top cell	1.08	20.6	74.1	16.5
Silicon IR cell	0.716	39.0	75.9	21.2
Filtered silicon IR cell	0.679	12.3	77.9	6.5
Sum				23.0

Experimental Section

Perovskite Solar Cell Fabrication: Hole transport layer poly(bis(4-phenyl)(2,4,6-trimethylphenyl)amine) (PTAA) film was deposited on ITO/glass by spin-coating 0.2 wt% PTAA in toluene at 4000 rpm for 35 s. The as-prepared film was then thermally annealed at 100 °C for 10 min. The MAPbI$_3$ films were fabricated by one-step spin coating with antisolvent extraction approach. The perovskite precursor solution was prepared by dissolving 460 mg PbI$_2$ and 159 mg MAI in 700 μL DMF and 78 μL DMSO. In order to improve the wetting property of MAPbI$_3$ precursor on PTAA film, the PTAA coated ITO substrate was pre-wetted by spinning 50 μL DMF at 4000 rpm for 5 s. Then 80 μL MAPbI$_3$ precursor solution was spun onto PTAA at 2000 rpm for 2 s and 4000 rpm for 20 s, the sample was drop-casted with 120 μL toluene at 8 s of the second-step spin-coating. Subsequently, the sample was annealed at 65 °C for 10 min and 100 °C for 10 min. The two-step MAPbI$_3$ films were fabricated by solvent annealing induced interdiffusion method as reported process.[24] The electron-transporter layer PCBM was coated by spinning 2 wt% PCBM in dichlorobenzene at 6000 rpm for 35 s and then annealed at 100 °C for 30 min. After that, 20 nm C$_{60}$ and 8 nm bathocuproine (BCP) was sequentially deposited by thermal evaporation. Finally, the semitransparent metal electrode was sequentially deposited with 1 nm Cu, 7 nm Au, and 40 nm BCP by thermal evaporation. For the control device, 80 nm Cu was deposited by thermal evaporation instead of semitransparent metal electrode. The working area of the perovskite solar cells was 7.5 mm^2.

Silicon Solar Cell Fabrication: N-type, float-zone, as-cut (100) wafers were used as starting substrates. Alkaline texturing was performed in potassium hydroxide (KOH) to produce random pyramids on both sides of the wafer, followed by RCA cleaning and a short dip in buffered oxide etch (BOE) before amorphous silicon (a-Si:H) deposition. Plasma-enhanced chemical vapor deposition (PECVD) was used to deposit nominally 7 nm of intrinsic a-Si:H–followed by a short hydrogen plasma treatment—on both sides of the wafer. 12 nm of p-type a-Si:H and 10 nm of n-type a-Si:H were deposited on the front and rear sides, respectively, by incorporating trimethylboron (TMB) and phosphine (PH$_3$) into the silane (SiH$_4$) precursor. On the front side, a 50 nm thick IZO layer was deposited by DC sputtering through a shadow mask to define 2 cm × 2 cm cells. Low-temperature silver paste was screen printed and annealed at 200 °C for 20 min, followed by deposition of 120 nm of silicon oxide (SiO$_x$) via PECVD. On the rear side, 15 nm of ITO was deposited by DC sputtering, followed by 300 nm of MgF$_2$ via thermal evaporation and 200 nm of silver via sputtering.

Device Characterization: Current–voltage measurements were carried out by a Keithley 2400 Source meter under simulated AM 1.5G irradiation (100 mW cm^{-2}), which was produced by a Xenon-lamp-based solar simulator (Oriel 67005, 150 W Solar Simulator). The scanning rate was 0.1 V s^{-1}. The steady-state photocurrent density and PCE of perovskite solar cell was measured at 0.87 V applied bias. The J–V curves of perovskite solar cells and silicon solar cells were measured separately. The silicon bottom cell size was 2.0 cm × 2.0 cm, and the characterization of filtered Si IR cell was carried out under simulated AM 1.5 G illumination after filtering by a 2.5 cm × 2.5 cm semitransparent perovskite cell from glass/ITO side. We measured the silicon solar cell

by adding a perovskite filter on top with a 2 mm air gap between the filter and silicon cell. This gap causes some reflection loss, and we expect slightly higher tandem efficiency if measuring with index-matching fluid between the perovskite and silicon cell. The transmittance, absorption, and reflectance were characterized with LAMBDA 950/1050 UV/VIS/NIR Spectrophotometer from Perkin Elmer. EQE curves were characterized with a Newport QE measurement kit by focusing a monochromatic beam of light onto the devices. The morphology images were acquired using tapping mode AFM (MFP3D, Asylum Research, USA). The SEM images were taken from a Quanta 200 FEG environmental scanning electron microscope.

Supporting Information

Supporting Information is available from the Wiley Online Library or from the author.

Acknowledgements

[1] W. S. Yang, J. H. Noh, N. J. Jeon, Y. C. Kim, S. Ryu, J. Seo, S. I. Seok, *Science* **2015**, *348*, 1234.

[2] H. P. Zhou, Q. Chen, G. Li, S. Luo, T. B. Song, H. S. Duan, Z. R. Hong, J. B. You, Y. S. Liu, Y. Yang, *Science* **2014**, *345*, 542.

[3] W. Chen, Y. Wu, Y. Yue, J. Liu, W. Zhang, X. Yang, H. Chen, E. Bi, I. Ashraful, M. Graetzel, L. Han, *Science* **2015**, *350*, 944.

[4] A. Kojima, K. Teshima, Y. Shirai, T. Miyasaka, *J. Am. Chem. Soc.* **2009**, *131*, 6050.

[5] NREL record solar cell efficiency table, http://www.nrel.gov/ncpv/images/efficiency_chart.jpg (accessed: April, 2016).

[6] J. Burschka, N. Pellet, S. J. Moon, R. Humphry-Baker, P. Gao, M. K. Nazeeruddin, M. Gratzel, *Nature* **2013**, *499*, 316.

[7] M. Z. Liu, M. B. Johnston, H. J. Snaith, *Nature* **2013**, *501*, 395.

[8] Q. Dong, Y. Fang, Y. Shao, P. Mulligan, J. Qiu, L. Cao, J. Huang, *Science* **2015**, *347*, 967.

[9] J. H. Noh, S. H. Im, J. H. Heo, T. N. Mandal, S. I. Seok, *Nano Lett.* **2013**, *13*, 1764.

[10] E. Edri, S. Kirmayer, D. Cahen, G. Hodes, *J. Phys. Chem. Lett.* **2013**, *4*, 897.

[11] N. K. Noel, S. D. Stranks, A. Abate, C. Wehrenfennig, S. Guarnera, A. A. Haghighirad, A. Sadhanala, G. E. Eperon, S. K. Pathak, M. B. Johnston, A. Petrozza, L. M. Herz, H. J. Snaith, *Energy Environ. Sci.* **2014**, *7*, 3061.

[12] Y. Ogomi, A. Morita, S. Tsukamoto, T. Saitho, N. Fujikawa, Q. Shen, T. Toyoda, K. Yoshino, S. S. Pandey, T. L. Ma, S. Hayase, *J. Phys. Chem. Lett.* **2014**, *5*, 1004.

[13] F. Hao, C. C. Stoumpos, D. H. Cao, R. P. H. Chang, M. G. Kanatzidis, *Nat. Photonics* **2014**, *8*, 489.

www.MaterialsViews.com

ADVANCED
ENERGY
MATERIALS

www.advenergymat.de

COMMUNICATION

[14] S. P. Pang, H. Hu, J. L. Zhang, S. L. Lv, Y. M. Yu, F. Wei, T. S. Qin, H. X. Xu, Z. H. Liu, G. L. Cui, *Chem. Mater.* **2014**, *26*, 1485.

[15] A. Mei, X. Li, L. Liu, Z. Ku, T. Liu, Y. Rong, M. Xu, M. Hu, J. Chen, Y. Yang, M. Grätzel, H. W. Han, *Science* **2014**, *345*, 295.

[16] J. W. Lee, D. J. Seol, A. N. Cho, N. G. Park, *Adv. Mater.* **2014**, *26*, 4991.

[17] G. E. Eperon, S. D. Stranks, C. Menelaou, M. B. Johnston, L. M. Herz, H. J. Snaith, *Energy Environ. Sci.* **2014**, *7*, 982.

[18] F. C. Hanusch, E. Wiesenmayer, E. Mankel, A. Binek, P. Angloher, C. Fraunhofer, N. Giesbrecht, J. M. Feckl, W. Jaegermann, D. Johrendt, T. Bein, P. Docampo, *J. Phys. Chem. Lett.* **2014**, *5*, 2791.

[19] Q. Chen, H. Zhou, Z. Hong, S. Luo, H. S. Duan, H. H. Wang, Y. Liu, G. Li, Y. Yang, *J. Am. Chem. Soc.* **2014**, *136*, 622.

[20] M. Xiao, F. Huang, W. Huang, Y. Dkhissi, Y. Zhu, J. Etheridge, A. Gray-Weale, U. Bach, Y.-B. Cheng, L. Spiccia, *Angew. Chem.* **2014**, *126*, 10056.

[21] J. H. Im, I. H. Jang, N. Pellet, M. Grätzel, N. G. Park, *Nat. Nanotechnol.* **2014**, *9*, 927.

[22] N. J. Jeon, J. H. Noh, Y. C. Kim, W. S. Yang, S. Ryu, S. Il Seol, *Nat. Mater.* **2014**, *13*, 897.

[23] Z. G. Xiao, C. Bi, Y. C. Shao, Q. F. Dong, Q. Wang, Y. B. Yuan, C. G. Wang, Y. L. Gao, J. S. Huang, *Energy Environ. Sci.* **2014**, *7*, 2619.

[24] Z. Xiao, Q. Dong, C. Bi, Y. Shao, Y. Yuan, J. Huang, *Adv. Mater.* **2014**, *26*, 6503.

[25] C. D. Bailie, M. G. Christoforo, J. P. Mailoa, A. R. Bowring, E. L. Unger, W. H. Nguyen, J. Burschka, N. Pellet, J. Z. Lee, M. Graetzel, R. Noufi, T. Buonassisi, A. Salleo, M. D. McGehee, *Energy Environ. Sci.* **2015**, *8*, 956.

[26] J. P. Mailoa, C. D. Bailie, E. C. Johlin, E. T. Hoke, A. J. Akey, W. H. Nguyen, M. D. McGehee, T. Buonassisi, *Appl. Phys. Lett.* **2015**, *106*, 121105.

[27] K. A. Bush, C. D. Bailie, Y. Chen, A. R. Bowring, W. Wang, W. Ma, T. Leijtens, F. Moghadam, M. D. McGehee, *Adv. Mater.* **2016**, *28*, 3937.

[28] S. Albrecht, M. Saliba, J. P. C. Baena, F. Lang, L. Kegelmann, M. Mews, L. Steier, A. Abate, J. Rappich, L. Korte, R. Schlatmann, M. K. Nazeeruddin, A. Hagfeldt, M. Graetzel, B. Rech, *Energy Environ. Sci.* **2016**, *9*, 81.

[29] L. Kranz, A. Abate, T. Feurer, F. Fu, E. Avancini, J. Loeckinger, P. Reinhard, S. M. Zakeeruddin, M. Graetzel, S. Buecheler, A. N. Tiwari, *J. Phys. Chem. Lett.* **2015**, *6*, 2676.

[30] J. Werner, C.-H. Weng, A. Walter, L. Fesquet, J. P. Seif, S. De Wolf, B. Niesen, C. Ballif, *J. Phys. Chem. Lett.* **2016**, *7*, 161.

[31] F. Fu, T. Feurer, T. Jaeger, E. Avancini, B. Bissig, S. Yoon, S. Buecheler, A. N. Tiwari, *Nat. Commun.* **2015**, *6*, 8932.

[32] D. P. McMeekin, G. Sadoughi, W. Rehman, G. E. Eperon, M. Saliba, M. T. Hoerantner, A. Haghighirad, N. Sakai, L. Korte, B. Rech, M. B. Johnston, L. M. Herz, H. J. Snaith, *Science* **2016**, *351*, 151.

[33] J. Werner, G. Dubuis, A. Walter, P. Loeper, S.-J. Moon, S. Nicolay, M. Morales-Masis, S. De Wolf, B. Niesen, C. Ballif, *Sol. Energy Mater. Sol. Cells* **2015**, *141*, 407.

[34] C. T. Zuo, H. J. Bolink, H. W. Han, J. S. Huang, D. Cahen, L. M. Ding, *Adv. Sci.* **2016**, 1500324.

[35] F. Guo, H. Azimi, Y. Hou, T. Przybilla, M. Hu, C. Bronnbauer, S. Langner, E. Spiecker, K. Forberich, C. J. Brabec, *Nanoscale* **2015**, *7*, 1642.

[36] Y. Yang, Q. Chen, Y.-T. Hsieh, T.-B. Song, N. De Marco, H. Zhou, *ACS Nano* **2015**, *9*, 7714.

[37] C. Roldan-Carmona, O. Malinkiewicz, R. Betancur, G. Longo, C. Momblona, F. Jaramillo, L. Camacho, H. J. Bolink, *Energy Environ. Sci.* **2014**, *7*, 2968.

[38] G. E. Eperon, V. M. Burlakov, A. Goriely, H. J. Snaith, *ACS Nano* **2014**, *8*, 591.

[39] Q. Wang, Y. C. Shao, Q. F. Dong, Z. G. Xiao, Y. B. Yuan, J. S. Huang, *Energy Environ. Sci.* **2014**, *7*, 2359.

[40] Y. H. Deng, Q. F. Dong, C. Bi, Y. B. Yuan, J. S. Huang, *Adv. Energy Mater.* **2016**, 1600372.

[41] C. Bi, Q. Wang, Y. Shao, Y. Yuan, Z. Xiao, J. Huang, *Nat. Commun.* **2015**, *6*, 7747.

[42] Y. X. Zhao, K. Zhu, *J. Am. Chem. Soc.* **2014**, *136*, 12241.

[43] L. K. Ono, S. Wang, Y. Kato, S. R. Raga, Y. Qi, *Energy Environ. Sci.* **2014**, *7*, 3989.

[44] J. H. Heo, S. H. Im, J. H. Noh, T. N. Mandal, C. S. Lim, J. A. Chang, Y. H. Lee, H. J. Kim, A. Sarkar, M. K. Nazeeruddin, M. Gratzel, S. I. Seok, *Nat. Photonics* **2013**, *7*, 487.

[45] L. Vitos, A. V. Ruban, H. L. Skriver, J. Kollar, *Surf. Sci.* **1998**, *411*, 186.

[46] Y. Zhou, M. Yang, W. Wu, A. L. Vasiliev, K. Zhu, N. P. Padture, *J. Mater. Chem. A* **2015**, *3*, 8178.

[47] N. Ahn, D.-Y. Son, I.-H. Jang, S. M. Kang, M. Choi, N.-G. Park, *J. Am. Chem. Soc.* **2015**, *137*, 8696.

[48] Y. C. Shao, Y. J. Fang, T. Li, Q. Wang, Q. F. Dong, Y. H. Deng, Y. B. Yuan, H. T. Wei, M. Y. Wang, A. Gruverman, J. E. Shield, J. S. Huang, *Energy Environ. Sci.* **2016**, *9*, 1752.

[49] Y. Shao, Z. Xiao, C. Bi, Y. Yuan, J. Huang, *Nat. Commun.* **2014**, *5*, 5784.

[50] J. M. Ball, S. D. Stranks, M. T. Hoerantner, S. Huettner, W. Zhang, E. J. W. Crossland, I. Ramirez, M. Riede, M. B. Johnston, R. H. Friend, H. J. Snaith, *Energy Environ. Sci.* **2015**, *8*, 602.

[51] S. D. Wolf, A. Descoeudres, Z. Holman, C. Ballif, *Green* **2012**, *2*, 7.

[52] M. Morales-Masis, S. M. De Nicolas, J. Holovsky, S. De Wolf, C. Ballif, *IEEE J. Photovoltaics* **2015**, *5*, 1340.

[53] D. L. Meier, D. K. Schroder, *IEEE Trans. Electron Dev.* **1984**, *31*, 647.

[54] Z. C. Holman, S. De Wolf, C. Ballif, *Light Sci. Appl.* **2013**, *2*, e106.

[55] Z. C. Holman, A. Descoeudres, S. De Wolf, C. Ballif, *IEEE J. Photovoltaics* **2013**, *3*, 1243.

[56] Z. C. Holman, M. Filipic, A. Descoeudres, S. De Wolf, F. Smole, M. Topic, C. Ballif, *J. Appl. Phys.* **2013**, *113*, 013107.